Title
Bouc–Wen class models considering hysteresis mechanism of RC columns in nonlinear dynamic analysis

Authors
Oh, Sebin
Kim, Taeyong
Song, Junho

Publication Date
2023

DOI
10.1016/j.ijnonlinmec.2022.104263

International Journal of Non-Linear Mechanics 148 (2023) 104263

Contents lists available at ScienceDirect

International Journal of Non-Linear Mechanics

journal homepage: www.elsevier.com/locate/nlm

Bouc–Wen class models considering hysteresis mechanism of RC columns in nonlinear dynamic analysis

Sebin Oh [a,1], Taeyong Kim [b,1], Junho Song [c,*]

[a] Department of Civil and Environmental Engineering, University of California, Berkeley, CA, United States of America
[b] Department of Civil and Mineral Engineering, University of Toronto, Toronto, Canada
[c] Department of Civil and Environmental Engineering, Seoul National University, Seoul, Republic of Korea

ARTICLE INFO

Keywords:
Bouc–Wen class model
Hysteretic behavior
Nonlinear dynamic analysis
Finite element analysis
Reinforced concrete (RC) column
Structural degradation

ABSTRACT

Bouc–Wen class models have been widely used to describe the hysteretic behaviors of structures in nonlinear dynamic and stochastic analyses. Since the existing Bouc–Wen class models cannot fully represent the hysteretic characteristics of reinforced concrete (RC) columns with structural degradation, the model fitted to the hysteresis loop from a specific input loading may not provide accurate response predictions under general loading conditions. To address this issue, we first identify two hysteresis mechanisms of RC columns, namely acute deterioration and pinching relaxation. Next, a new Bouc–Wen model is proposed to describe the hysteresis mechanisms based on the modified Bouc–Wen–Baber–Noori (m-BWBN) model. The proposed model considers the hysteresis mechanisms by two additional parameters, which are adequately bounded to facilitate the parameter identification process. Two different input loadings, i.e., a monotonically increasing one and the other with a sudden increase and decrease of the amplitude, are introduced to investigate the effects of the input loading patterns on the model calibration. The fitted models are applied to predict the responses under a quasi-static cyclic loading and a real earthquake ground motion. The effectiveness of the proposed model is demonstrated by comparison with nonlinear finite element analyses of RC columns in a database. While the m-BWBN and the proposed model show good agreements in the model calibration, only the proposed model calibrated by the input loading with sudden amplitude changes successfully predicts the responses of degrading RC columns. The proposed model will contribute to highly efficient and accurate predictions by nonlinear dynamic and stochastic analyses of a degrading structure modeled by an equivalent single-degree-of-freedom system.

1. Introduction

Nonlinear hysteretic systems are widely used in mechanical, robotics, geotechnical, and civil engineering fields. However, their path-dependent relationship between deformation and resisting force makes the performance evaluation challenging. In particular, it is hard to predict the hysteretic behavior of a reinforced concrete (RC) structure because of its large uncertainties in the material properties. Since a dynamic or stochastic analysis with a full-scale three-dimensional finite element model would demand high computational costs, many researchers have used an equivalent single-degree-of-freedom (SDOF) hysteretic system to represent an RC structure or subsystem [1–5].

Such hysteretic models are classified into polygonal hysteresis models (PHMs) and smooth hysteresis models (SHMs) [6]. The PHMs, e.g., the elasto-plastic model [7] and Ibarra pinching hysteresis model [1], are widely used because the physical implications of the model parameters are intuitive and thus make the model identification convenient. On the other hand, SHMs utilizing differential equations are mathematically versatile and tractable [8] and facilitate nonlinear stochastic analyses.

One of the most widely used SHMs is the Bouc–Wen class model, initially developed by Bouc [9] and later generalized by Wen [10]. The Bouc–Wen class models have been applied to various engineering problems because the models require only one auxiliary nonlinear differential equation to describe the hysteretic behavior. Moreover, such mathematical tractability enables closed-form expressions for the coefficients of the equivalent linear system, which facilitates the use of the Bouc–Wen class model in nonlinear stochastic analyses [11,12]. In particular, the Bouc–Wen–Baber–Noori (BWBN) model [13] has gained immense popularity because it can describe a large variety of hysteresis shapes of RC components, including pinching effects and degradation in stiffness and strength. Several researchers validated the applicability

* Corresponding author.
E-mail address: junhosong@snu.ac.kr (J. Song).
[1] Equal contribution first authors.

https://doi.org/10.1016/j.ijnonlinmec.2022.104263
Received 15 May 2022; Received in revised form 2 October 2022; Accepted 4 October 2022
Available online 13 October 2022

of the BWBN model by calibrating the model to experimental data of various RC structures, including frames [14], beam–column joints [15], walls [16], and columns [6,17,18].

The fact that the model has shown a satisfying agreement with specific experimental data does not guarantee that the calibrated model can predict the equivalent resisting force for general input displacement time histories [19]. The functional redundancy inherent in the existing Bouc–Wen class models leads to the lack of robustness in the prediction over general loading conditions [8,20,21]. In addition, the parameters of the Bouc–Wen class models do not necessarily describe the physical meaning inherent in the hysteresis [20], which can serve as a significant source of the functional redundancy. Thus, for a reliable prediction of the hysteretic behavior of an RC structure, the model parameters should be able to describe its hysteresis mechanisms effectively and concisely. However, the mechanisms have been investigated using a limited number of similar loading conditions suggested by several guidelines and design codes [22–25]. Therefore, a thorough investigation of the hysteresis of RC structures using various loading histories is needed.

This study aims to develop a Bouc–Wen class model that can consider the hysteresis mechanism of RC columns in nonlinear dynamic analysis. To this end, we first characterize two hysteresis mechanisms of RC columns that the existing Bouc–Wen class models cannot fully describe. After carefully examining the mathematical formulations of the existing Bouc–Wen class models, a new Bouc–Wen class model is developed by incorporating the suggested features into the mathematical formulation through two additional model parameters. We specify bounds for each model parameter and explain the parameter identification procedure in detail to promote practical applications. Moreover, an algorithm for estimating the resisting force given an input displacement vector and a dynamic analysis method using the proposed model are provided in the appendices. Next, the extended coverage of the newly proposed model is examined by calibrating the model to the results of nonlinear finite element (FE) analyses of RC column test cases. The proposed model's prediction performance under a quasi-static cyclic load and a dynamic load of seismic excitation is tested and demonstrated compared to an existing model. Concluding remarks and discussions are provided at the end regarding further research on the proposed model and its applications.

2. Review: BWBN and m-BWBN models

2.1. Bouc–Wen–Baber–Noori (BWBN) model

The modeling approach based on an idealized SDOF system is widely used to simulate structural responses under stochastic excitations, especially during the design phase [26–28]. In such an approach, a structural system, e.g., frame structure, is simplified in terms of a global degree of freedom or modeled as an assembly of SDOF systems representing interconnected elements, e.g., beams and columns. The following second-order nonhomogeneous ordinary differential equation describes such an idealized SDOF system subjected to dynamic excitations:

$$m\ddot{u} + c\dot{u} + f_s(u,\dot{u}) = F(t) \tag{1}$$

where u, $\dot{u}$, and $\ddot{u}$ respectively denote the relative displacement, velocity, and acceleration of the system; m is the mass; c is the viscous damping coefficient; $F(t)$ is the time-dependent forcing function; and f_s is the resisting force describing the force–deformation relationship. The Bouc–Wen class models describe the hysteretic behavior of a structural element by introducing a hysteretic displacement z to the resisting force in Eq. (1) in the form

$$f_s(u,z) = \alpha k_0 u + (1-\alpha) k_0 z \tag{2}$$

where α is the post-to-preyield stiffness ratio; and k_0 is the initial stiffness. Note that the resistant force is elastic if $\alpha = 1$, and purely inelastic if $\alpha = 0$. Fig. 1 illustrates an equivalent hysteretic SDOF system described by a Bouc–Wen class model.

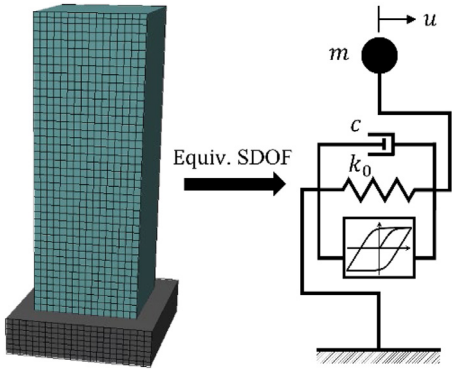

Fig. 1. Modeling a hysteretic structure by an equivalent SDOF system using a Bouc–Wen class model.

Among various Bouc–Wen class models, a Bouc–Wen–Baber–Noori (BWBN) model is widely used to represent the hysteretic behavior of RC structural elements owing to its capability to describe the stiffness/strength deteriorations and pinching effects [13,19]. The hysteretic displacement z in the BWBN model follows a nonlinear differential equation

$$\dot{z} = \frac{h(z,\varepsilon)}{\eta(\varepsilon)}\dot{u}\left[A - |z|^n(\gamma + \beta\,\mathrm{sgn}(\dot{u}z))\,\nu(\varepsilon)\right] \tag{3}$$

where $h(z,\varepsilon)$, $\eta(\varepsilon)$, and $\nu(\varepsilon)$ are the functions of the cumulative energy ε, introduced to describe the pinching effect and degradations in stiffness and strength degradations, respectively; A is the scale parameter; n controls the sharpness of the yielding transition; β and γ are the basic shape parameters describing hardening and softening, respectively; and $\mathrm{sgn}(\cdot)$ is the signum function. The cumulative hysteretic energy ε follows the rate equation

$$\dot{\varepsilon} = (1-\alpha) k_0 z\dot{u} \tag{4}$$

Compared to the Bouc–Wen model [9,10], $h(z,\varepsilon)$, $\eta(\varepsilon)$, and $\nu(\varepsilon)$ are newly introduced in the BWBN model. The degradation functions $\eta(\varepsilon)$ and $\nu(\varepsilon)$ are defined as linear functions of ε as follows:

$$\eta(\varepsilon) = 1 + \delta_\eta \varepsilon \tag{5}$$

$$\nu(\varepsilon) = 1 + \delta_\nu \varepsilon \tag{6}$$

where δ_η and δ_ν determine the rates of degradations in stiffness and strength, respectively. The pinching function takes the form

$$h(z,\varepsilon) = 1 - \zeta_1(\varepsilon)\exp\left(-\frac{\left(z\cdot\mathrm{sgn}(\dot{u}) - q z_u\right)^2}{\zeta_2^2(\varepsilon)}\right) \tag{7}$$

in which q controls the pinching initiation; $z_u = \left(\frac{A}{\nu(\beta+\gamma)}\right)^{1/n}$ is the ultimate value of z; and $\zeta_1(\varepsilon)$ and $\zeta_2(\varepsilon)$ represent the progress of pinching as

$$\zeta_1(\varepsilon) = \zeta_0\left(1 - \exp(-p\varepsilon)\right) \tag{8}$$

$$\zeta_2(\varepsilon) = \left(\psi + \delta_\psi\right)\left(\lambda + \zeta_1(\varepsilon)\right) \tag{9}$$

where ζ_0 is a measure of the total slip; p controls the rate of the initial drop in the slope; ψ relates to the pinching magnitude; δ_ψ contributes to the rate of pinching; and λ controls the variation of the functions $\zeta_1(\varepsilon)$ and $\zeta_2(\varepsilon)$. Although the stiffness and strength degradations are respectively controlled by δ_η and δ_ν as shown in Eqs. (5) and (6), the pinching effect is governed by a set of parameters: p, q, ζ_0, ψ, δ_ψ, and λ. Note that the pinching phenomenon is not considered when $h(z,\varepsilon) = 1$.

In summary, the BWBN model has 14 parameters: $\{\alpha,\ k_0,\ A,\ \beta,\ \gamma,\ n,\ \delta_\eta,\ \delta_\nu,\ p,\ q,\ \zeta_0,\ \psi,\ \delta_\psi,\ \lambda\}$. The parameters of the BWBN model

are known to be functionally redundant, i.e., there exist multiple sets of parameters that can produce an identical hysteresis loop [8,20,21]. Several studies have adopted a constraint on A being 1 to alleviate this issue. However, such constraint still does not guarantee the identified parameter set to be unique to the hysteretic characteristics of a given structural element. This redundancy issue will be further handled in the new model proposed in Section 4. (By adopting the constraint $A = 1$, the number of parameters used in the BWBN model is reduced to 13.)

2.2. Modified Bouc–Wen–Baber–Noori (m-BWBN) model

Although the BWBN model can effectively describe various hysteretic characteristics of structures, it cannot explicitly control the yield strength of hysteresis, i.e., determined by the combination of the 13 parameters. Since the yield strength determines the level of nonlinearity of structures under seismic excitation, it is essential to explicitly adjust it for an effective simulation of the force–deformation relationship. Kim [19] and Kim et al. [29] addressed this issue by proposing a modified Bouc–Wen–Baber–Noori (m-BWBN) model, in which the resisting force f_s in Eq. (2) is altered to

$$f_s(u,z) = \alpha k_0 u + (1-\alpha) F_y z \tag{10}$$

where F_y denotes the yield force of a system. Thereby, the hysteretic displacement z is given as a unitless variable. For consistency with Eq. (10), Eqs. (3) and (4) are modified to

$$\dot{z} = \frac{h(z,\varepsilon)}{\eta(\varepsilon)}\dot{u}\left[A - |z|^n(\gamma + \beta \mathrm{sgn}(\dot{u}z))\nu(\varepsilon)\right]\frac{k_0}{F_y} \tag{11}$$

$$\dot{\varepsilon} = (1-\alpha) F_y z \dot{u} \tag{12}$$

All the other model parameters are the same as those in the BWBN model.

Substituting u in Eq. (10) for the yield displacement $u_y = F_y/k_0$, we find that z_u must be 1 to guarantee that the resisting force $f_s(u,z)$ is set as F_y at the yield point. It is noted from $z_u = (A/\nu(\beta+\gamma))^{1/n}$ that, when there is no strength degradation, i.e., $\nu(\varepsilon) = 1$, the ultimate value of z is $z_u = (1/\beta+\gamma)^{1/n}$. Therefore, the additional constraint $\beta + \gamma = 1$ is introduced in the m-BWBN model to assure F_y as the yield strength of the structure [19,29].

As a result, the m-BWBN model has a total of 13 independent parameters: $\{\alpha,\ k_0,\ F_y,\ \beta$ (or $\gamma)$, $n,\ \delta_\eta,\ \delta_\nu,\ p,\ q,\ \zeta_0,\ \psi,\ \delta_\psi,\ \lambda\}$. Kim [19] proposed a two-step procedure for adequately identifying the parameters of the m-BWBN model either from refined FE models or from experiments. First, the three most important parameters, α, k_0, and F_y are identified from the monotonic force–deformation relationship, i.e., pushover curve. Next, the other parameters describing the details of the inelastic behavior are determined using the results of a quasi-static cyclic analysis. Compared to the BWBN model, the m-BWBN model with the two-step identification procedure shows better prediction accuracy and reduces the computational costs required to find the optimal parameter set [19].

3. Hysteresis mechanisms of RC columns

3.1. Acute deterioration

The difference in the strengths of concrete and reinforcement steel causes the deterioration of RC columns under cyclic loading. When RC columns are subjected to relatively small lateral forces, both concrete and steel resist the lateral forces. However, a repeated cyclic loading or a large amount of lateral force may incur a significant loss of the lateral resistance capacity of the concrete. As a result, if the concrete exceeds its yield strength, an RC column's deterioration level may change even under similar loading conditions. Therefore, such a hysteresis mechanism should be reflected in the hysteretic energy part of the BWBN or m-BWBN model to accurately simulate the degradation in RC columns.

The relationship between the degradation level and the hysteretic energy is identified by comprehensive computational simulations of an RC column subjected to a cyclic loading using the nonlinear finite element analysis program VecTor2. The VecTor2's capability to describe the hysteretic behaviors of RC columns has been proved in previous research [30–33]. The FE models used in this study generate hysteresis loops nearly identical to those obtained from the actual experiments, as presented in Section 5.2. Fig. 2(a) shows a typical hysteresis loop of an RC column with strength degradation, simulated by VecTor2. The loading history applied for the hysteresis loop is shown in the upper left corner of the figure, in which A, B, C, and D stand for the maximum displacement δ_0 of the first, second, third, and fourth cycles, respectively. To investigate the level of strength degradation, Fig. 2(b) shows the hysteresis in the red square of Fig. 2(a). The maximum force at δ_0 has deteriorated as the cyclic loading proceeds. However, the level of deterioration between A and B is different from that of B and C, or C and D. From the stress–strain analysis of each fiber in the numerical model, we found that both reinforcement and concrete resist the lateral forces at A, while the lateral forces are resisted primarily by the reinforcement steel at B, C, and D. In other words, once the concrete loses its functionality in terms of lateral resistance, the strength deterioration of the RC column is mainly determined by that of steel.

However, in the hysteretic energy, such an acute deterioration arising from the loss of resistance capacity in concrete is not distinguished from the gradual deterioration in steel. The cumulative hysteretic energy over the load steps in Fig. 2(c) shows that the differences between the hysteretic energy at the four points, i.e., the differences between ε_A, ε_B, ε_C, and ε_D, are comparable, which contradicts the trends of the deterioration level shown in Fig. 2(b). Since the acute deterioration appears obviously under loading conditions entailing a sharp change in deformation, such as near-fault ground motions, it is desirable to modify the mathematical formulation of the m-BWBN model to accurately simulate the hysteretic behaviors of RC columns under general excitations. The modification proposed for incorporating the acute deterioration is presented in Section 4.1.

3.2. Pinching relaxation

The pinching effect refers to a sudden loss of stiffness, primarily caused by damage of structural components [13]. The occurrence of pinching is often associated with a shear lock, reinforcement slippage, and crack closure in RC columns [18]. Pinching stems from the mutual relationship between reinforcement and concrete and the effective area's change due to the crack's opening and closure. Therefore, the pinching effect may not be observed under a relatively small external force even after the RC columns have experienced prominent cyclic behaviors, i.e., cracks have already been developed, because no crack openings or closures will occur in such cases. Investigating such a "pinching relaxation" phenomenon is essential because the seismic loading generally shows nonstationary behaviors.

To further elaborate on the pinching relaxation, Fig. 3 shows a typical hysteresis of an RC column showing the pinching effect from the RC simulation model. The displacement steps for the hysteresis are provided in the upper left corner of Fig. 3, where A and B respectively denote the maximum and minimum peaks corresponding to the first and the last cycles. In the figure, the slope of the unloading path from the peak of relatively large deformation, e.g., point A, is determined initially by the stiffness degradation. After that, the pinching effect occurs as the unloading path goes toward the origin, making the slopes decrease sharply. On the other hand, when the peak deformation is relatively small, e.g., point B, the stiffness during the unloading path is determined by the stiffness degradation, and the pinching effect is hardly observed over the whole path. Since the level of the pinching effect is affected by the opening and closure of cracks, the pinching effect does not appear during the unloading path from small peak

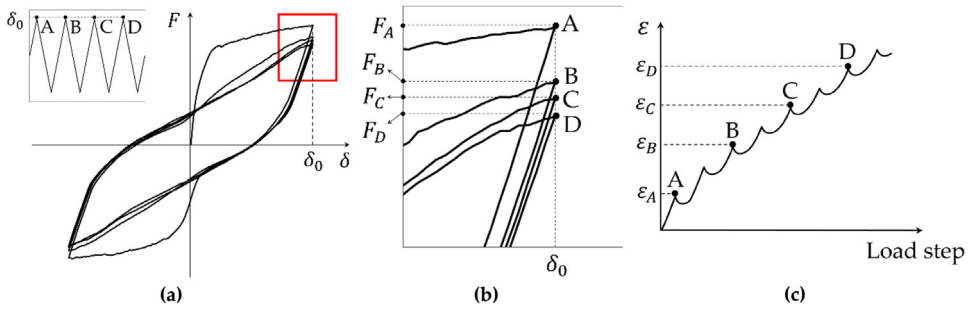

Fig. 2. Illustration of inconsistency between degradation and hysteretic energy: (a) typical hysteresis loop showing strength degradation obtained by the repeated cyclic load shown in the upper left; (b) the magnified view for the red box in Fig. 2(a); and (c) the cumulative hysteretic energy over the load steps.

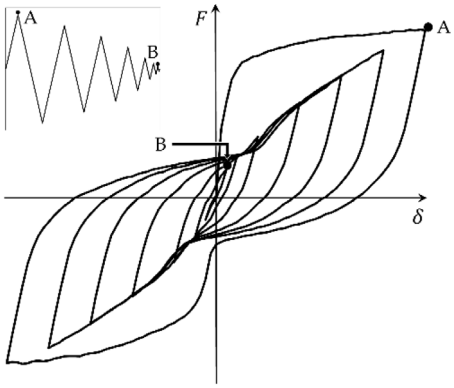

Fig. 3. A typical hysteresis loop obtained under the loading history in the upper left.

deformations that cannot open a sufficient amount of cracks. In other words, the stiffness of the RC column within relatively small peak deformations is governed primarily by the stiffness degradation parameters even after a significant deterioration has occurred in the column. Note that according to the m-BWBN model, as shown in Eq. (11), the stiffness of hysteresis is governed by stiffness deterioration $\eta(\varepsilon)$ and pinching effect $h(z,\varepsilon)$ within the small z values where the pinching effect takes place.

The pinching relaxation cannot be described by the mathematical formulation of the m-BWBN model. According to Eq. (7), the pinching function is determined by z, ζ_1, and ζ_2. In addition, from Eqs. (8) and (9), we can find that ζ_1 and ζ_2 asymptotically reach their limits and become constants as the cumulative hysteretic energy ε increases. This implies that the pinching function h becomes a univariate function of the hysteretic displacement z when a significant amount of hysteretic energy ε has been accumulated, i.e., the element has experienced a large amount of deterioration. Thereby, in the m-BWBN model, the pinching effect is involved whenever z is small enough.

Fig. 4(a) provides a general illustration of the pinching mechanism used in the m-BWBN model. The color in the figure describes the severity of the pinching effect: the pinching effect is severe in the red areas ($h(z,\varepsilon) \approx 0$) and does not occur in the black areas ($h(z,\varepsilon) = 1$). Under such a mechanism, as shown in Fig. 4(b), the m-BWBN model cannot simulate the pinching relaxation presented in Fig. 3. Fig. 4(b) shows the numerical test results using a Bouc–Wen class model that is calibrated for the hysteresis loop presented in Fig. 3. In this numerical example, to examine the pinching relaxation only, a parameter $c_{\bar{\varepsilon}}$ that describes the acute deterioration (details are covered in Section 4.1.1) is added to the m-BWBN model. To highlight the inability of the m-BWBN model in describing the pinching relaxation, the corresponding hysteresis loop obtained from the FE analysis software VecTor2 is presented in a gray dashed line (which is equivalent to Fig. 3), while the severity of pinching is visualized by color to be consistent with Fig. 4(a). In Fig. 4(b), the magnitude of the pinching function depends only on the value of z, as illustrated in Fig. 4(a). According to such a univariate mechanism, the stiffness at the same z values should decrease along the displacement steps due to the stiffness degradation, especially within small z values where the stiffness is governed only by the pinching effect and stiffness degradation. However, it contradicts the actual trend of stiffness observed from comprehensive numerical tests denoted by the gray dashed lines. In Fig. 4(b), for example, the stiffness at the points crossing the x-axis which shows a similar level of pinching function increases as the load proceeds, owing to the pinching relaxation. The modification proposed for incorporating the pinching relaxation is presented in Section 4.2.

4. Proposed Bouc–Wen class model

A new Bouc–Wen class model is developed to describe the two hysteresis mechanisms: acute deterioration and pinching relaxation. To this end, two additional parameters are introduced. The hysteresis from the new Bouc–Wen model, i.e., the hysteretic force for the given displacement step, can be obtained using the algorithm presented in Appendix A.

4.1. Mathematical formulations

4.1.1. Consideration of acute deterioration

The m-BWBN model describes the deterioration level using a function of the cumulative hysteretic energy, as shown in Eqs. (5) to (9). As discussed in Section 3.1, the equations cannot adequately describe the acute deterioration. Therefore, a deterioration energy term is newly introduced to replace the cumulative hysteretic energy in defining the deterioration level and pinching effects. Since different crack propagations can be developed for both positive and negative moments along with the external load cycles, the deterioration energy is defined in positive (push) and negative (pull) directions, respectively. Given the fact that the acute deterioration occurs when the structure experiences a deformation larger than the previous maximum deformation, the following mathematical description is proposed by adopting the Heaviside step function $\mathrm{H}(\cdot)$ for the difference between the current and the maximum displacements in both directions that the RC column has experienced:

$$\dot{\bar{\varepsilon}}_+ = \left(1 + c_{\bar{\varepsilon}} \cdot \mathrm{H}\left(u - u_{\max}\right)\right)\dot{\varepsilon} = \left(1 + c_{\bar{\varepsilon}} \cdot \mathrm{H}\left(u - u_{\max}\right)\right)(1-\alpha)\,F_y z \dot{u} \quad (13)$$

$$\dot{\bar{\varepsilon}}_- = \left(1 + c_{\bar{\varepsilon}} \cdot \mathrm{H}\left(u_{\min} - u\right)\right)\dot{\varepsilon} = \left(1 + c_{\bar{\varepsilon}} \cdot \mathrm{H}\left(u_{\min} - u\right)\right)(1-\alpha)\,F_y z \dot{u} \quad (14)$$

where $\dot{\bar{\varepsilon}}_+$ and $\dot{\bar{\varepsilon}}_-$ respectively denote the derivatives of the deterioration energy for the positive and negative directions under the cyclic loading; $u_{\max}$ and $u_{\min}$ are the previous maximum and minimum displacements, respectively (Note that $u_{\min}$ implies the maximum deformation in the negative direction but is denoted as the minimum considering the negative sign.); and $c_{\bar{\varepsilon}}$ is an amplification factor newly introduced to amplify the deterioration energy when the current displacement is larger than the previous maximum displacement or smaller than the

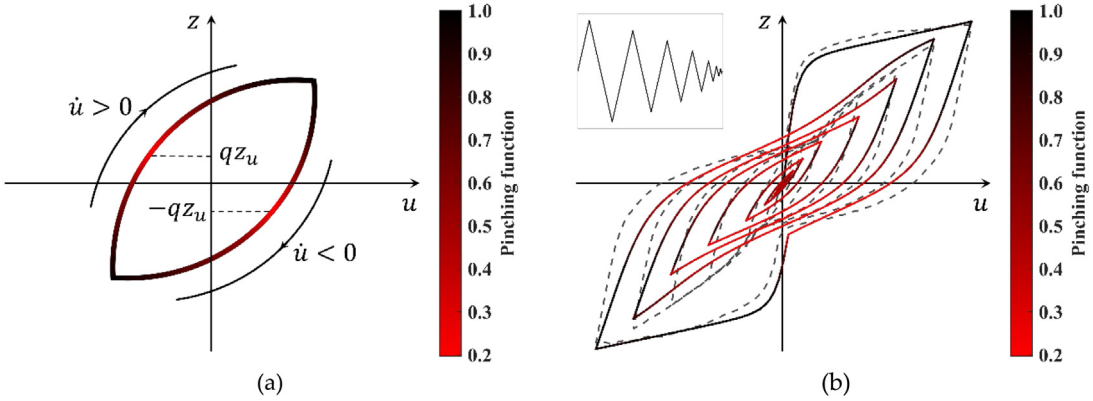

Fig. 4. Demonstration of the pinching mechanism in the existing models for two examples: (a) general hysteresis loop; and (b) the calibration result using the hysteresis loop in Fig. 3. (For interpretation of the references to color in this figure legend, the reader is referred to the web version of this article.)

previous minimum displacement. It is noted that the rate equation of the m-BWBN model is used in Eqs. (13) and (14).

By introducing another Heaviside function, the positive and negative deterioration energies are combined to determine the deterioration energy

$$\tilde{\varepsilon} = \tilde{\varepsilon}_{+} \cdot \mathrm{H}(u) + \tilde{\varepsilon}_{-} \cdot (1 - \mathrm{H}(u)) \tag{15}$$

which supersedes the cumulative hysteretic energy ε in Eqs. (5) to (9). By introducing the amplification factor and the Heaviside step functions, it is possible to properly consider the effects of the displacement increments in the deterioration and pinching effects. It is also noted that Eq. (15) is equivalent to Eq. (12) when $c_{\tilde{\varepsilon}} = 0$.

4.1.2. Consideration of pinching relaxation

As discussed in Section 3.2, the pinching relaxation is determined by the deformation at the previous peak. To consider this mechanism, the pinching relaxation function h_r is newly introduced as a function of the deformation of the previous peak as follows:

$$h_r(u_p) = 1 - \exp\left(-c_h \cdot \frac{|u_p|}{u_y}\right) \tag{16}$$

where c_h is a pinching relaxation coefficient, which is newly introduced in this study; u_y is the yield displacement of the system that can be defined as F_y/k_0; and u_p is the last peak displacement. To define u_p mathematically, the set of load steps corresponding to the peaks up to the load step i is first defined as

$$\mathcal{P}_i = \left\{ j \,|\, |u_j| > |u_{j-1}| \cap |u_j| > |u_{j+1}| \right\} \quad \text{for } j \in \{1, 2, \ldots, i-1\} \tag{17}$$

Therefore, the set $\mathcal{P}_i$ contains all load steps up to the ith one for which the displacement exhibits a local maximum in magnitude. The last peak displacement is then given simply by

$$u_{p_i} = u_{\max \mathcal{P}_i} \tag{18}$$

in which u_{p_i} is the last peak displacement at the ith load step. In Eq. (16), c_h controls the level of pinching relaxation; and u_p is normalized by u_y to make h_r a unitless variable. Eq. (16) is designed to guarantee the following conditions: (1) h_r always lies between 0 and 1 by introducing an exponential function, and (2) the effect of material/sectional properties of RC columns is considered by c_h. These conditions enable the proposed model to incorporate the inherent pinching mechanism into the mathematical expression and become the original model when the pinching relaxation is hardly observed in the element. Finally, h_r is combined with the original pinching function h as follows to describe the pinching relaxation:

$$h(z, \tilde{\varepsilon}) = 1 - \zeta_1(\tilde{\varepsilon}) \exp\left(-\frac{\left(z \cdot \mathrm{sgn}(\dot{u}) - qz_u\right)^2}{\zeta_2^2(\tilde{\varepsilon})}\right) h_r(u_p) \tag{19}$$

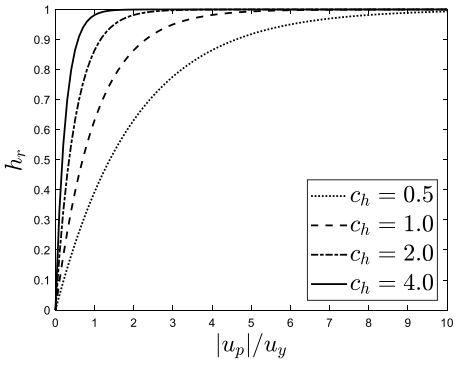

Fig. 5. Realizations of the pinching relaxation function h_r for four different values of pinching relaxation coefficient c_h.

Table 1
Summary of the model parameters: roles and bounds.

No.	Parameter	Role	Bounds
1	α	Post-yield stiffness ratio	$0 \le \alpha \le 0.5$
2	k_0/m	Normalized initial stiffness	$0.04 \le k_0/m \le 1,600$ [s^{-2}]
3	F_y/m	Normalized yield force	$0.05\mathrm{g} \le F_y/m \le 1.5\mathrm{g}$
4	β (or γ)	Basic hysteretic shape control	$0 \le \beta \le 1$ (or $0 \le \gamma \le 1$)
5	n	Sharpness of yield	$1 \le n \le 5$
6	δ_η	Stiffness degradation ratio	$0 \le \delta_\eta \le 0.39$
7	δ_ν	Strength degradation ratio	$0 \le \delta_\nu \le 0.36$
8	p	Pinching slop	$0 \le p \le 1.38$
9	q	Pinching initiation	$0.01 < q \le 0.43$
10	ζ_0	Measure of total slip	$0 \le \zeta_0 < 1$
11	ψ	Pinching magnitude	$0.1 \le \psi \le 0.85$
12	δ_ψ	Pinching rate	$0 \le \delta_\psi \le 0.09$
13	λ	Pinching severity	$0.01 \le \lambda \le 0.8$
14	$c_{\tilde{\varepsilon}}$	Deterioration energy amplification	$0 \le c_{\tilde{\varepsilon}} \le 200$
15	c_h	Pinching relaxation	$0.05 \le c_h \le 3.0$

Note that the deterioration energy $\tilde{\varepsilon}$ replaces ε in Eq. (7).

To further examine the role of the pinching relaxation coefficient, Fig. 5 shows the four realizations of the suggested pinching relaxation function with $|u_p|/u_y$ for four different values of c_h. A large value of c_h makes the pinching relaxation function reach near 1.0 at a relatively small u_p. This indicates that the element does not involve the pinching relaxation phenomenon.

In summary, Eqs. (13), (14), and (16) introduce two new parameters, which makes the proposed Bouc–Wen model has a total of 15 parameters: $\{\alpha, k_0, F_y, \beta \text{ (or } \gamma), n, \delta_\eta, \delta_\nu, p, q, \zeta_0, \psi, \delta_\psi, \lambda, c_{\tilde{\varepsilon}}, c_h\}$. The roles of the parameters in the existing models and the proposed model are summarized in Table 1.

4.2. Bounds on model parameters

An ideal approach to determining the bounds of the model parameters for RC columns is to examine many parameter sets calibrated using the data from either numerical simulations or actual experiments. However, since it is arduous to obtain such a large volume of data for hysteresis loops, Kim [19] proposed bounds for all parameters of the m-BWBN model based on the Structural Performance Database [34] compiled by the Pacific Earthquake Engineering Research Center (PEER). The database covers 416 RC columns subjected to quasi-static cyclic tests. Kim [19] used a genetic algorithm to identify the model parameters from each experimental dataset. We adopt the bounds proposed by Kim [19] for the parameters of the proposed Bouc–Wen class model, except $c_{\bar{\varepsilon}}$ and c_h that are newly introduced in this study. For $c_{\bar{\varepsilon}}$ and c_h, the bounds are determined basically by physical reasoning and complemented by comprehensive numerical investigations. The upper bound of c_h is determined as 3.0 so that the pinching relaxation function $h_r = 1 - \exp(-c_h \cdot |u_p| \,/\, u_y)$ is larger than 0.95 when $|u_p| = u_y$. Although not explicitly linked, such an upper bound implies that more than 95% of cracks are opened when the last peak displacement equals the yield displacement. The lower bound for $c_{\bar{\varepsilon}}$ is set to 0, which means no acute deterioration. The remaining bounds for $c_{\bar{\varepsilon}}$ and c_h are determined by fitting the parameters to the PEER database using a genetic algorithm. The bounds for all parameters of the proposed Bouc–Wen class model are summarized in Table 1, where g is the gravitational acceleration. Note that the bounds for the normalized initial stiffness are compatible with the range for typical natural periods of civil and architectural structures of 0.05 s to 10 s.

4.3. Parameter identification procedure for proposed Bouc–Wen class model

Parameter identification of hysteresis models is a global optimization problem that seeks the optimal values of a set of parameters that replicate the given input force–displacement relationship, i.e., hysteresis loop. For the proposed Bouc–Wen class model, we aim to identify the values of the parameter vector $\boldsymbol{\theta} = [\alpha, k_0, F_y, \beta, n, \delta_\eta, \delta_\nu, p, q, \zeta_0, \psi, \delta_\psi, \lambda, c_\varepsilon, c_h]^{\mathrm{T}}$ that minimize the objective function

$$OF(\boldsymbol{\theta}) = \frac{1}{N}\left[\sum_{i=1}^{N}\left(f_s(i) - \hat{f}_s(i|\boldsymbol{\theta})\right)^2\right]^{1/2} \tag{20}$$

where N is the number of the data points or loading steps; $f_s(i)$ denotes the resisting force measured from the experiment at the ith loading step; and $\hat{f}_s(t_i|\boldsymbol{\theta})$ represents the resisting force at the ith loading step predicted by the proposed Bouc–Wen class model with the parameter set $\boldsymbol{\theta}$. The parameter identification problem is then formulated as a nonlinear single-objective optimization problem of minimizing $OF(\boldsymbol{\theta})$ while satisfying the constraints by the lower and upper bounds specified in Table 1.

In this study, we solve the optimization problem using a genetic algorithm, widely used in parametric identification for Bouc–Wen class models [15,17,35]. The genetic algorithm identifies the best solution through the following three phases: crossover, mutation, and selection. Each *generation* consisting of the three steps continues until the population yields a lower fitness value than the pre-specified tolerance or the population converges to a specific parameter set. More details of the generic-algorithm-based identification of Bouc–Wen class model parameters can be found in [17] and [19]. Following Kim [19], one modification has been made in the mutation step from the standard genetic algorithm such that the level of randomness decreases as the iteration proceeds. This modification introduces the simulated annealing effect [36], which can increase the population's diversity and prevent a premature convergence to local minima.

Table 2
Statistics of the 253 RC columns used for numerical investigations (Std.: standard deviation, CoV: coefficient of variation).

Column property	Max	Min	Mean	Std.	CoV
Depth (mm)	914.4	80	301.6	118.2	0.392
Aspect ratio	7.638	1	3.438	1.384	0.403
Axial load ratio	0.9	0	0.265	0.197	0.742
Longitudinal steel ratio, ρ_l (%)	6.03	0.68	2.374	1.003	0.423
Transverse steel ratio, ρ_s (%)	6.7	0	1.018	1.136	1.116

5. Numerical investigations

Tests on the performance of the proposed Bouc–Wen class model require the force–deformation data of a wide variety of RC columns under various types of loading histories. To this end, a nonlinear finite element analysis program VecTor2 was used. In addition, experimental datasets for RC columns are adopted from the Structural Performance Database [34] compiled by the Pacific Earthquake Engineering Research Center (PEER). The following subsection provides the details of the modeling procedures, followed by the results of the numerical investigation.

5.1. Experimental data in structural performance database

A total of 416 sets of experimental data are available in the PEER database. The database consists of 253 rectangular-shaped and 163 spiral-shaped RC columns. In addition to the results for quasi-static cyclic loading tests, i.e., the measured lateral loads and the global deformations at the tip, the details for the column and the experiment are specified in the database, including material properties, reinforcement layout, geometric properties, experimental configurations, and failure type of each column. All the load–deformation data from various test configurations are reduced to the case of an equivalent cantilever column for consistent comparisons of the columns.

Among the available 416 datasets, 253 rectangular-shaped RC columns are used to evaluate the performance of the proposed model. The influences of the axial load on the lateral load, i.e., P-Δ effects, are removed according to each loading configuration. The details for the loading configurations and the procedure to remove the P-Δ effect can be found in [34]. Table 2 summarizes key statistics of the rectangular-shaped RC columns used in this study, including aspect ratio, axial load ratio, and longitudinal and transverse reinforcement ratios. The percentages of the three failure types, flexure, shear, and flexure-shear, are 78.7%, 7.11%, and 14.2%, respectively.

5.2. Finite element models for reinforced concrete columns

For comprehensive numerical investigations, this study uses a nonlinear finite element analysis program, VecTor2, which is specialized in analyzing two-dimensional RC structures based on the Modified Compression-Field Theory [37] and the Distributed Stress Field Model [38,39]. The performance of VecTor2 has been demonstrated by the accurate simulation of the behavior of numerous RC structures under quasi-static or dynamic loading conditions [30–33,40]. In this study, we used the default constitutive laws of concrete and reinforcement steel provided by the VecTor2 (The details of the default settings can be found in the program manual [41]). The FE model uses four-node quadratic elements whose size range from 10 mm to 30 mm depending on the column's dimensions while keeping the height-to-width ratio below 1.5. The size of the elements is determined to ensure at least 15 elements along the transverse and the longitudinal directions.

A typical example of the constructed FE model is shown in Fig. 6. The longitudinal reinforcements are shown as vertical lines, while the transverse reinforcements, i.e., stirrup steels, are smeared with the core concrete. The axial and lateral loads are imposed through a steel loading plate to prevent an unrealistic local failure on concrete elements

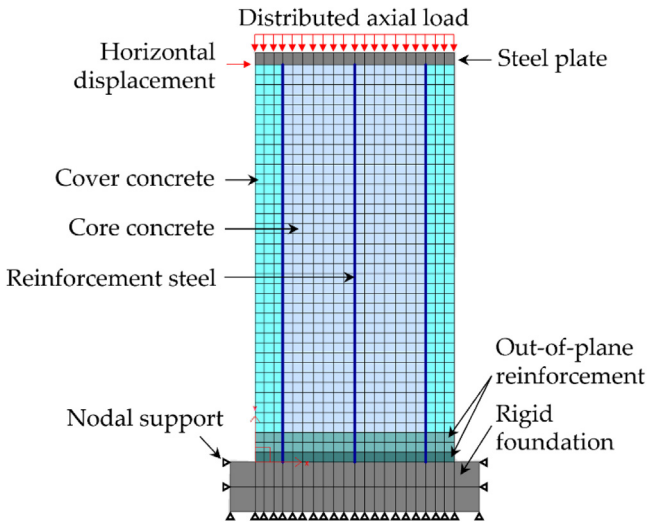

Fig. 6. A typical FE model for an RC column using VecTor2. (For interpretation of the references to color in this figure legend, the reader is referred to the web version of this article.)

from stress concentration. In addition, to represent the out-of-plane confinement effects in the concrete near the support plane, out-of-plane reinforcements are added to the neighboring elements so that the ductility of the FE models can reach that of the experimental data without shear failures near the support plate. This calibration technique has often been used to ensure the ductility of FE models, despite some strength enhancement [33]. The dark green and light green elements near the foundation represent the confined concrete with the additional out-of-plane reinforcement of 5% and 2.5%, respectively.

In this way, we constructed 253 FE models, 50 of which were compared to the actual experimental data to confirm the validity of the constructed FE models. Fig. 7 shows the force–deformation relationships of six representative FE models representing RC columns showing flexural, shear, and flexural-shear failures (2 for each failure type). The FE analysis results show good agreements with the experimental data from the PEER database. These six models will be presented as benchmark examples in the following numerical investigations.

For performance assessment of the constructed FE models, their hysteretic energies are compared to those in the experimental dataset, as in the previous studies [6,17]. Fig. 8 shows a scatter plot of the hysteretic energies obtained from the experimental and FE analyses for 50 out of 253 RC columns. The points representing 50 columns are distributed around the diagonal line in the figure, which implies that the FE models well describe the hysteretic behaviors of the corresponding RC columns.

5.3. Model calibrations

Two different cyclic input loadings in Fig. 9 are used to examine the performances of the m-BWBN model and the proposed model in simulating realistic hysteresis loops. The input loading in Fig. 9(a) is the one recommended in the report from the American Concrete Institute [22], which has been commonly used for RC structures. The input loading in Fig. 9(b) is introduced to investigate the simulating capacity of the models under the loading histories distinct from the conventional one. In particular, the second input loading shows a sudden increase in amplitude and revisits the elastic region.

The parameters of the proposed and the m-BWBN models are identified for 253 RC columns by the procedure described in Section 4.3. Fig. 10 shows the force–displacement data obtained under the first input loading for the six benchmark models presented in Fig. 7. The calibrated m-BWBN and proposed models are shown by the blue dashed and the red dashed lines in Fig. 10, respectively. Both models show a reasonable agreement with the FE analysis results. Moreover, the calibration results of all 253 RC columns are checked in terms of hysteretic energy, as shown in Fig. 11. The satisfying performances of the two models for the first input loading can also be found in the scatter plots as the points are distributed along the diagonal.

Similarly, the model parameters are identified using the second input loading in Fig. 9(b). Both models show a reasonable agreement with the FE analysis results, as shown in Figs. 12 and 13. However, it is noteworthy that the proposed model fits overall better. The superior performance is prominent in simulating hysteresis of the RC columns showing flexural failure, which are the two cases on the left side of Fig. 12. The proposed model provides more robust performance in model calibration against cyclic loading histories.

It should be noted that reasonable agreements with the hysteresis loops under specific input loadings do not necessarily imply that the fitted model represents the actual hysteresis mechanisms. Especially for the first input loading, the parameters associated with the acute deterioration and the pinching relaxation might not be accurately identified because the input loading does not cause such hysteretic behaviors. It is, however, noted that such hysteretic characteristics are observed under different loading conditions (see Fig. 12) and should be considered to accurately predict the seismic responses of RC columns. Therefore, in the next subsection, the calibrated models are tested in terms of their capability to predict responses under quasi-static and dynamic loading histories.

5.4. Response predictions

The following four models are tested: (1) m-BWBN model calibrated with the first input loading; (2) proposed model calibrated with the first input loading; (3) m-BWBN model calibrated with the second input loading; and (4) proposed model calibrated with the second input loading. Those four models will be referred to as M1, P1, M2, and P2 for brevity.

The following two loads are used to explore their response prediction capabilities: (1) a quasi-static cyclic load different from the loading histories used for the model calibration; and (2) a dynamic load of seismic acceleration. Fig. 14(a) shows the quasi-static cyclic load compatible with an envelope function widely used for generating artificial ground motions [42]. Fig. 14(b) presents the acceleration record of the 1940 El Centro earthquake.

First, Figs. 15 and 16 represent the quasi-static response prediction results of M1 and P1, respectively, for the six benchmark RC columns. M1 tends to overestimate the cumulative hysteretic energy. The numerical experiments by FE analysis show acute deterioration in the first cycle among the three cycles with the largest amplitude. However, the three cycles simulated by M1 show a comparable level of deterioration (in terms of the amount of reduced area). Moreover, especially for the RC columns showing flexural failure (the two subplots on the left sides of Figs. 15 and 16), M1 underestimates the stiffness during the cycles of decreasing amplitudes. The univariate pinching mechanism described in terms of z contradicts the FE results showing a larger stiffness after a sufficient amount of deterioration due to the pinching relaxation. Such tendency is hardly observed in the other four RC columns experiencing shear or flexural-shear failures. This may be attributed to the small-to-moderate magnitude of amplitudes used for those specimens. Even a small amount of damage can lead the column to collapse in shear-failure or flexural-shear failure RC columns. Therefore, a large magnitude of deformations that produces many cracks could not occur, which prevents the pinching relaxation stemming from crack opening and closure.

On the other hand, the proposed model calibrated with the first input loading (P1) provides quasi-static response predictions closer to the numerical experiment results. In particular, the hysteretic energy overestimation issue is alleviated. However, the stiffness underestimation issue during the cycles of decreasing amplitudes remains unresolved,

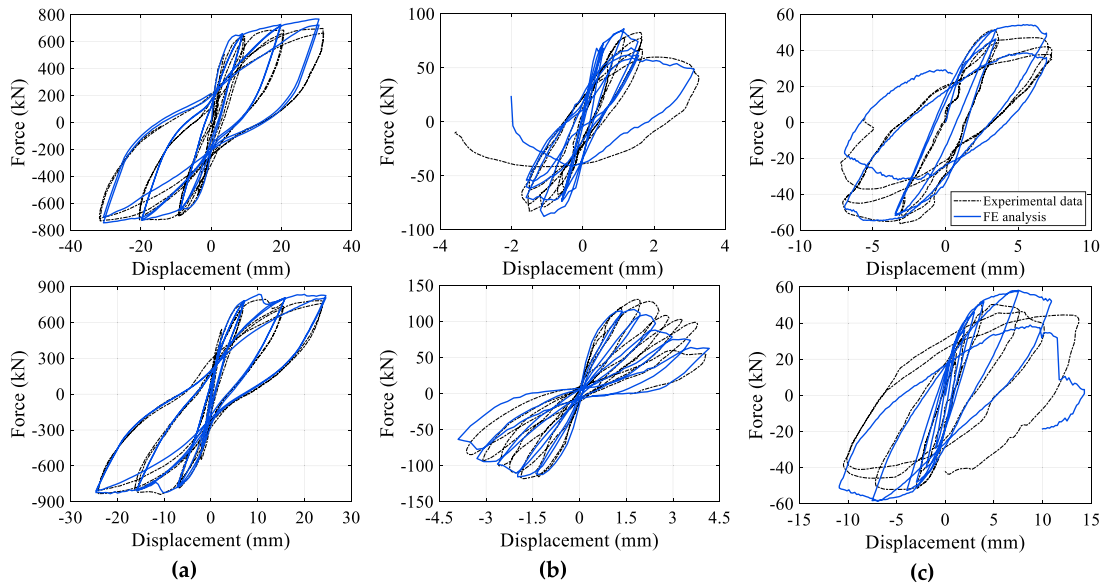

Fig. 7. Force–displacement relationships for six RC columns (two for each of the three failure types) obtained using the FE analysis compared to the experimental data: (a) flexural failure; (b) shear failure; and (c) flexural-shear failure.

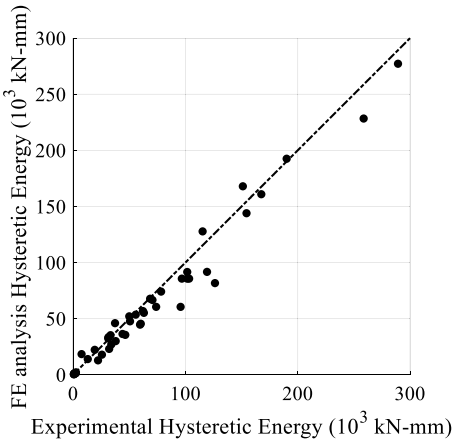

Fig. 8. Hysteretic energy by the FE analyses and the experiments.

which implies that P1 fails to consider the pinching relaxation. Although the proposed model can describe the pinching relaxation, the related parameters cannot be adequately identified in P1 because the first input loading in Fig. 9(a) does not have amplitude-decreasing cycles. In addition, the hysteresis loop of P1 during such cycles is excessively thin compared to the FE results and underestimates the hysteretic energy. As demonstrated later, this issue exacerbates the response prediction under a dynamic load.

Similarly, Figs. 17 and 18 show the results using M2 and P2, respectively. The hysteretic energy overestimation issue is alleviated by calibrating the models with the loading condition containing a sudden increase in amplitudes. However, the stiffness underestimation issue within small deformations remains in the m-BWBN model, while the proposed model accurately predicts the stiffness.

As a summary of the quasi-static response prediction results for the 253 RC columns, Fig. 19 presents the four models' normalized deviations of the hysteretic energies. In calculating the energies, the loading history is divided into the increasing and decreasing parts to investigate each model's coverage of acute deterioration and pinching relaxation. Fig. 19(a) shows that M1 significantly overestimates the hysteretic energy. In contrast, the other three models accurately predict the hysteretic energy within about a 10% error rate. The decent performance of P1 demonstrates the robust prediction capability of the proposed model against the selected input loading. On the other hand, the m-BWBN models significantly underestimate the energy in the decreasing-amplitude part for both loading protocols. Such an error is somewhat alleviated in P1 and further mitigated in P2. The quasi-static response prediction results from Figs. 15 to 19 confirm that the prediction performance of the proposed model is superior to the m-BWBN model and less sensitive to the input loading used for the model calibration.

Next, the dynamic analysis results using SDOF systems modeled by the four models are compared to those by FE simulations. To this end, VecTor2 is used with the Rayleigh damping and the implicit constant acceleration method. The damping ratio for the first mode is set to 2% and large damping ratios are assigned to higher modes (e.g., 40%) to simulate the dynamic behavior of the RC columns to ensure the numerical stability for dynamic analyses in VecTor2 [32,43]. Subsequently, an equivalent damping ratio for the SDOF system is determined based on the first mode damping ratio in VecTor2. However, a more direct comparison could be made between the responses of the SDOF system and the FE model if the damping ratio can be set as zero. For SDOF systems, the Runge–Kutta methods of orders four and five solve the equation of motions given in Eq. (1). Appendix B details the dynamic analysis using an SDOF system with the proposed model.

Fig. 20 shows the response time histories under the El Centro earthquake predicted using the four models for the first RC column in Fig. 7(a). The response time histories predicted using the P1 and P2 models match the FE analysis results well. In contrast, the stiffness underestimation issue of M1 and M2 shown in Figs. 15 and 17 results in the overestimated displacements shown in the left two plots in Fig. 20, respectively. Next, Fig. 21 provides the histograms of the global errors for the 253 RC columns. The global error for the dynamic response prediction is defined as the root mean square error (RMSE) between the displacement time histories of the FE models and the corresponding Bouc–Wen class models. Fig. 21 and Table 3 confirm that the prediction performances of P1 and P2 are superior to those of M1 and M2.

The scatter plots in Fig. 22 confirm that P1 tends to underestimate the hysteretic energy while P2 provides unbiased predictions. This tendency of P1 arises from the excessively thin hysteresis loop during the cycles after a large amount of deterioration (see Fig. 16). P1 shows a good prediction regarding the overall trajectories during seismic excitation since it can describe hysteretic behaviors of RC columns subjected to a sudden deformation increase, which takes a

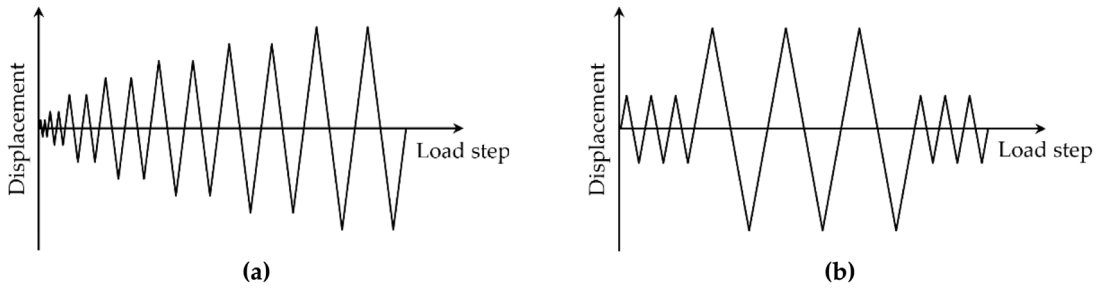

Fig. 9. Two cyclic input loadings used for model calibrations: (a) first input loading; and (b) second input loading.

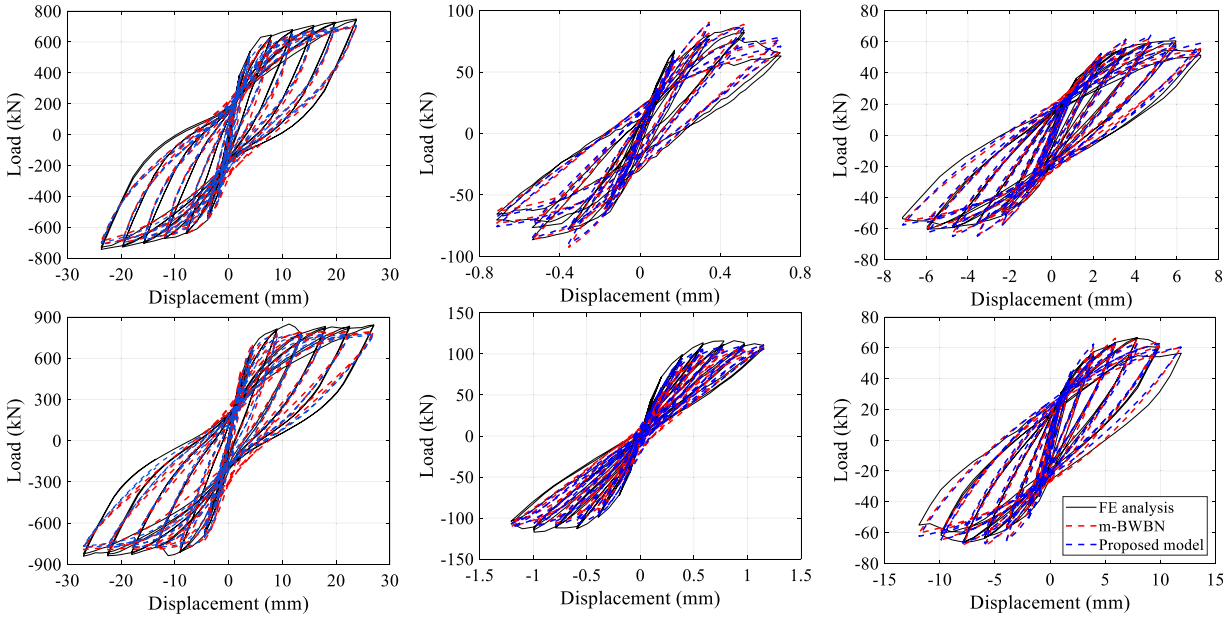

Fig. 10. Comparison of hysteresis loops under the first input loading obtained from the FE analyses and the calibrated hysteretic models. (For interpretation of the references to color in this figure legend, the reader is referred to the web version of this article.)

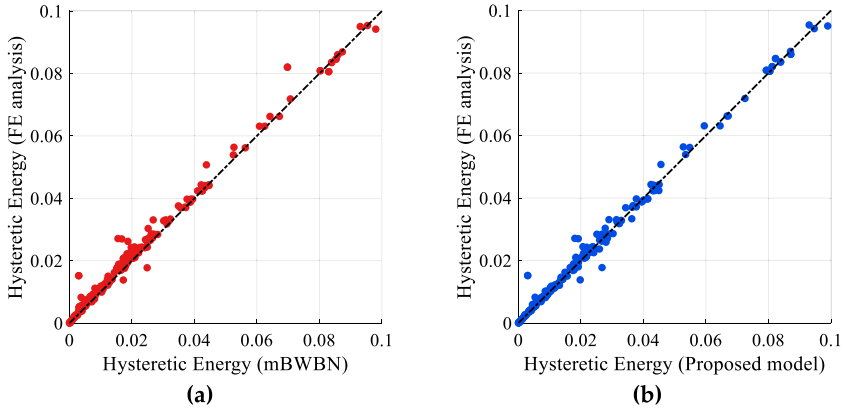

Fig. 11. Scatter plots of the hysteretic energies (unit: 10^3 kN mm) obtained from the FE analyses and the hysteretic models under the first input loading: (a) m-BWBN model; and (b) proposed model.

large part in calculating the global error. However, the deficiency in describing the behaviors after a loading history incurring a significant deterioration may hamper a reliable dynamic response prediction. In contrast, P2 shows satisfying prediction results for the overall trajectories and the hysteretic energy. These results indicate that a reliable prediction of quasi-static and dynamic responses by an equivalent SDOF system requires (1) a Bouc–Wen class model that can describe the target phenomenon, and (2) a loading protocol that facilitates adequate identification of the related model parameters. The proposed model identified by the second input loading (P2) satisfies both conditions and thus provides superb performance in response predictions.

6. Conclusions

Aiming to improve the predictive performance of the Bouc–Wen class models for RC columns under general loading conditions, this

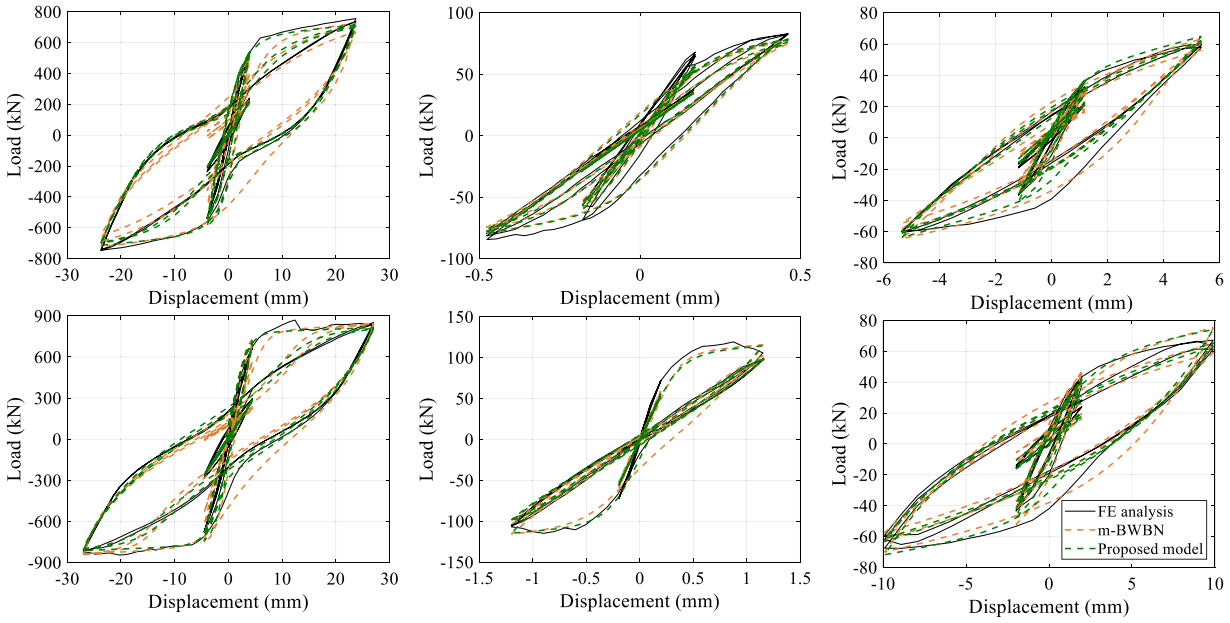

Fig. 12. Comparison of hysteresis loops under the second input loading obtained from the FE analyses and the calibrated hysteretic models. (For interpretation of the references to color in this figure legend, the reader is referred to the web version of this article.)

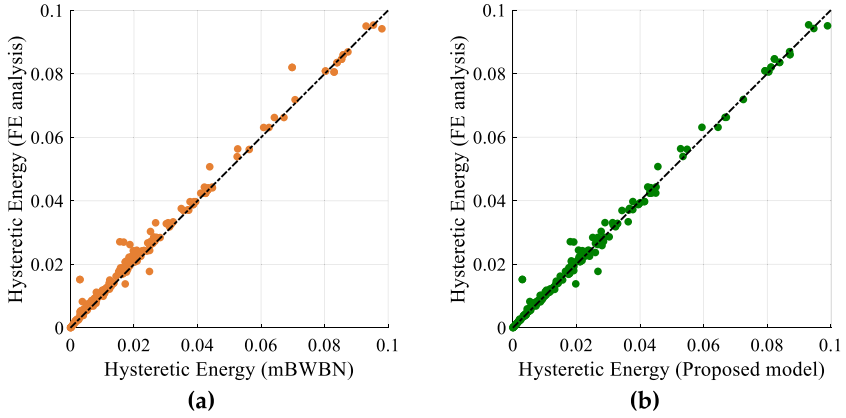

Fig. 13. Scatter plots of the hysteretic energies (unit: 10^3 kN mm) obtained from the FE analyses and the hysteretic models under the second input loading: (a) m-BWBN model; and (b) proposed model.

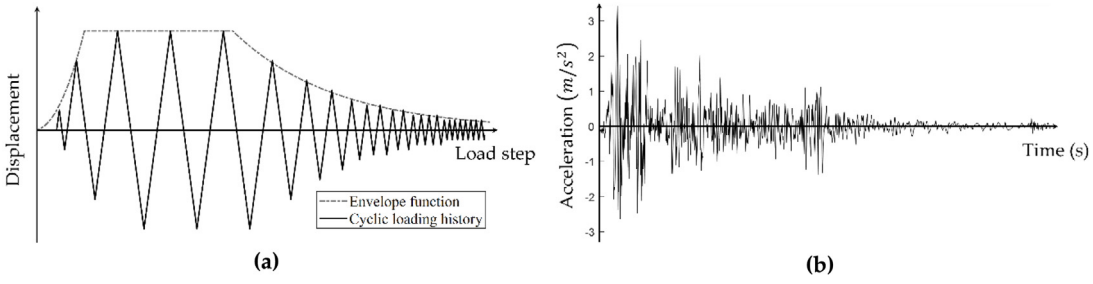

Fig. 14. Two cyclic loading histories used for response predictions: (a) a quasi-static cyclic load; and (b) a dynamic load of the El Centro acceleration.

study first identified two hysteretic characteristics that the existing Bouc–Wen class models could not describe effectively — acute deterioration and pinching relaxation. Based on a thorough examination of the hysteresis mechanisms, we introduced two parameters into the m-BWBN model by Kim [19]. The bounds of the model parameters and the detailed identification procedure were provided for practical use of the proposed model. A numerical algorithm for estimating the resisting force given displacement vector was also provided in Appendix A.

Numerical investigations using nonlinear finite element analyses of RC column cases in an experimental database demonstrated the proposed model's capabilities in model calibrations and response predictions. For model calibrations, two different input loadings are used to test the consistent predictive accuracy of the m-BWBN and proposed models. Both models provided suitable matches with the FE analysis results for both input loadings, while the m-BWBN model showed a slight difference. Based on the calibrated models, the responses of

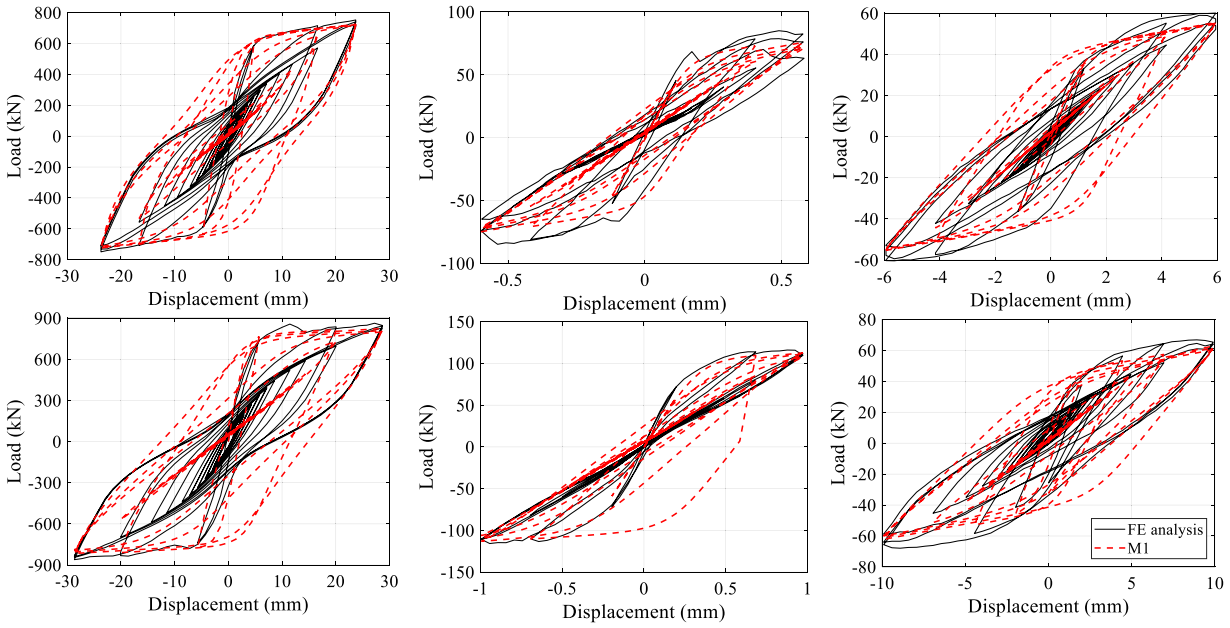

Fig. 15. Response prediction results of the m-BWBN model calibrated with the first input loading (M1) under the quasi-static cyclic load.

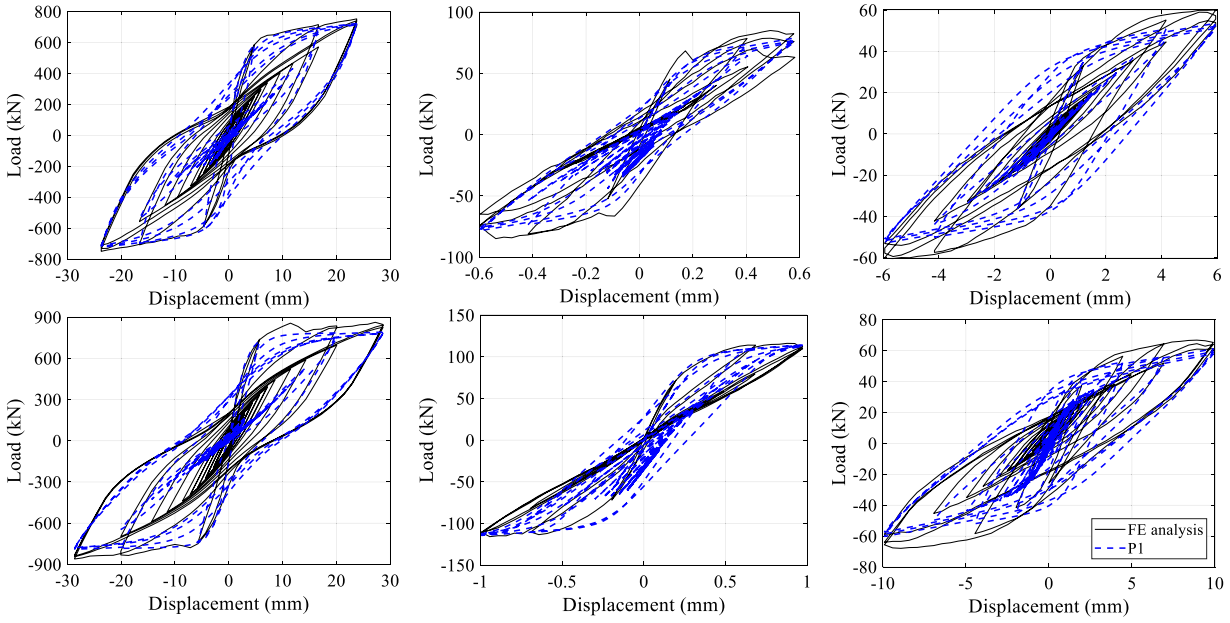

Fig. 16. Response prediction results of the proposed model calibrated with the first input loading (P1) under the quasi-static cyclic load.

Table 3
Statistics for the histograms by the four models in Fig. 21 (RMSE: root mean square error, and Std.: standard deviation).

Model	RMSE (mm)		
	Mean	Median	Std.
M1	5.824	3.831	4.761
P1	3.371	2.178	3.745
M2	6.121	4.793	4.738
P2	3.140	2.111	3.103

RC columns were predicted under a quasi-static cyclic load and the ground acceleration time histories of the El Centro earthquake. The proposed model showed good agreements for the quasi-static cyclic load no matter which input loading was used for the model calibration. In contrast, the m-BWBN model could not provide accurate response prediction results. Furthermore, the proposed model calibrated with the input loading showing sudden increase and decrease in the amplitude showed the most accurate results in terms of the overall trajectories and cumulative hysteretic energy for the El Centro earthquake.

The findings in this study widen the possibility of future research. To reduce the impact of the additional functional redundancy of the Bouc–Wen model from the introduced parameters, an effective and robust parameter identification technique is needed with a general input loading cycle. By developing a robust protocol that captures holistic hysteretic characteristics of structural elements and systems, the performance of the proposed Bouc–Wen class model and the existing ones can be further improved. Although this paper focuses on hysteretic behaviors of RC columns, the proposed Bouc–Wen class model could be used for various structural elements composed of materials having different mechanical properties.

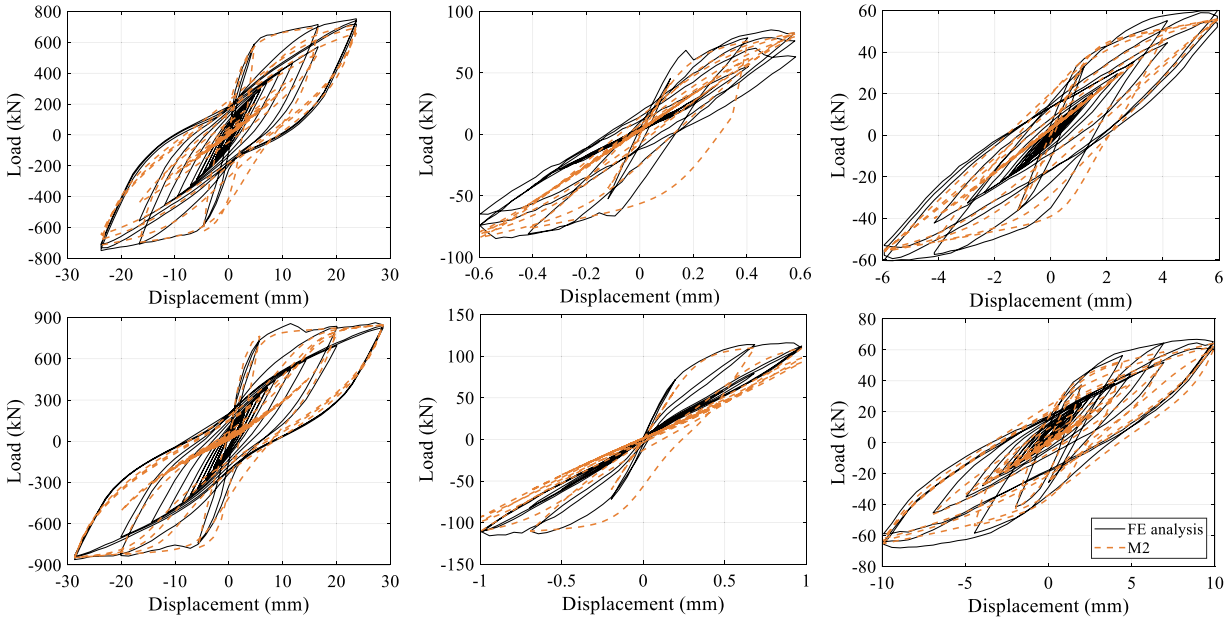

Fig. 17. Response prediction results of the proposed model calibrated with the second input loading (M2) under the quasi-static cyclic load.

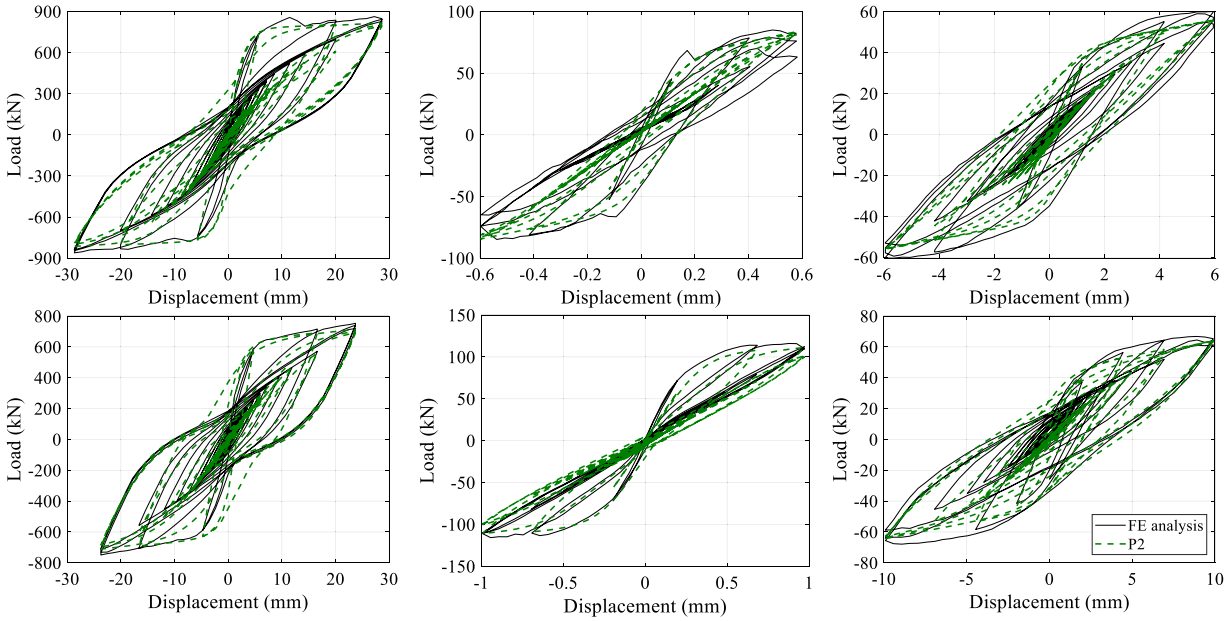

Fig. 18. Response prediction results of the proposed model calibrated with the second input loading (P2) under the quasi-static cyclic load.

CRediT authorship contribution statement

Sebin Oh: Conceptualization, Methodology, Investigation, Validation, Formal analysis, Data curation, Software, Visualization, Writing – original draft. **Taeyong Kim:** Conceptualization, Methodology, Investigation, Validation, Formal analysis, Software, Visualization, Writing – review & editing. **Junho Song:** Supervision, Research Overview, Methodology, Investigation, Validation, Formal analysis, Visualization, Funding acquisition, Writing – review & editing.

Declaration of competing interest

The authors declare that they have no known competing financial interests or personal relationships that could have appeared to influence the work reported in this paper.

Data availability

Data will be made available on request.

Acknowledgments

The first and the third authors are supported by the Korea Agency for Infrastructure Technology Advancement (KAIA) grant funded by the Ministry of Land, Infrastructure and Transport (Grant 22RMPP-C163162-02). The first author is also supported by Korea Ministry of Land, Infrastructure and Transport (MOLIT) as 『Innovative Talent Education Program for Smart City』. The second author is supported by Basic Science Research Program through the National Research Foundation of Korea (NRF) funded by the Ministry of Education (No. 2021R1A6A3A03040353). The third author is supported by the Institute of Engineering at Seoul National University.

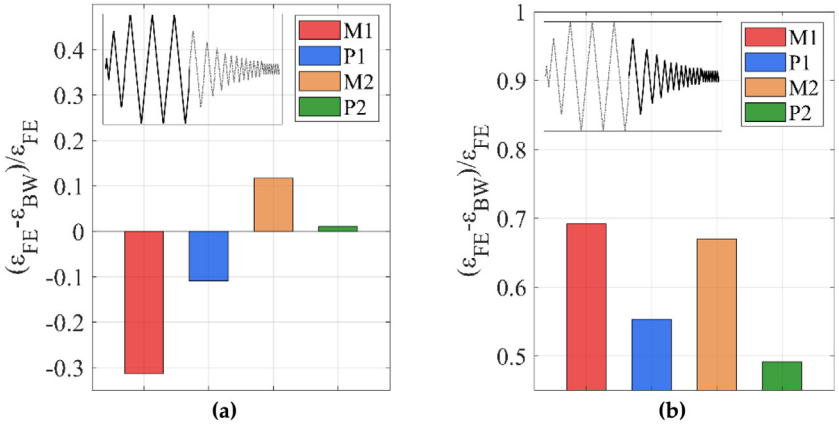

Fig. 19. Normalized deviations of hysteretic energy by the four models for (a) the amplitude-increasing part; and (b) the amplitude-decreasing part of the quasi-static loading history. (ϵ_{FE} and ϵ_{BW} stand for the hysteretic energies calculated from the FE analyses and the Bouc–Wen class models, respectively. (For interpretation of the references to color in this figure legend, the reader is referred to the web version of this article.))

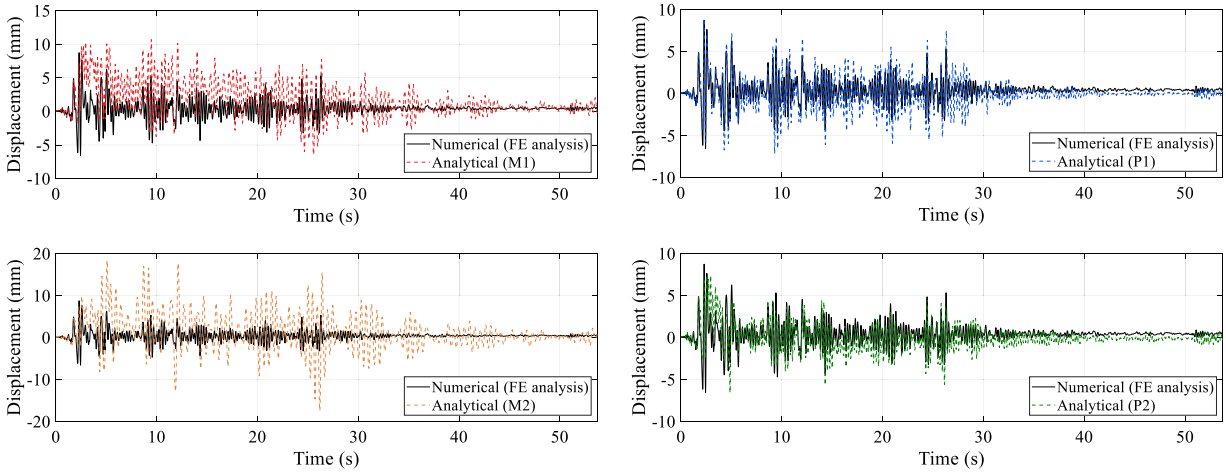

Fig. 20. Time histories under the El Centro earthquake predicted by the four models compared with FE analysis results.

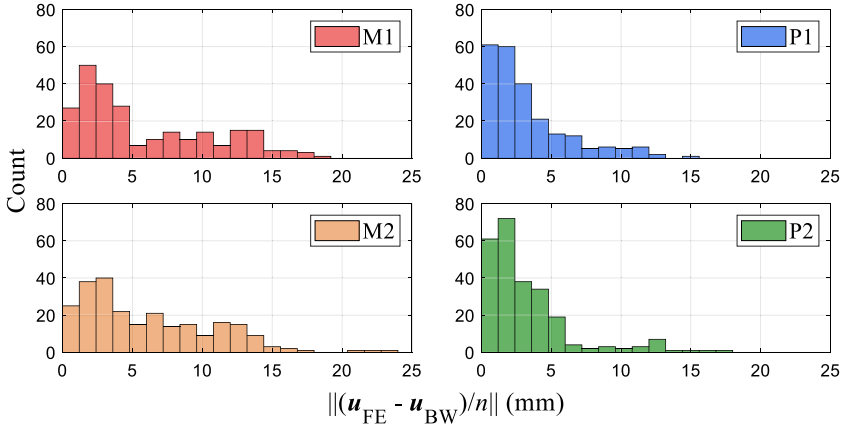

Fig. 21. Histograms of the global error for the 253 columns, predicted by the four models. ($\boldsymbol{u}_{FE}$ and $\boldsymbol{u}_{BW}$ denote the vector with the displacements obtained from the FE analysis and the Bouc–Wen models, respectively, as elements, n represents the number of time step, and $\|\cdot\|$ indicates the norm of the argument.)

Appendix A. Algorithm to determine the resisting force of the proposed Bouc–Wen class model

In analyses using the proposed model, the resisting forces given displacement steps are determined incrementally based on the algorithms previously developed for other Bouc–Wen class models [18,19,44,45].

From Eq. (10), the resisting force f_s at time t_{i+1} is expressed in incremental form as follows:

$$f_{s_{i+1}} = \alpha k_0 u_{i+1} + (1-\alpha) F_y z_{i+1} \tag{A.1}$$

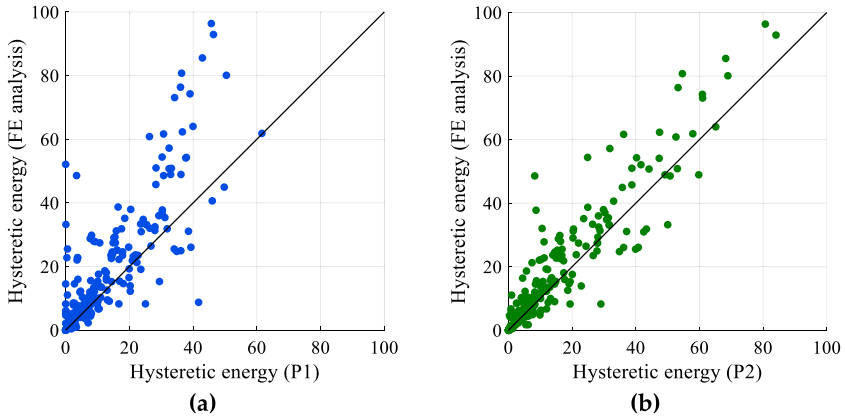

Fig. 22. Scatter plots of hysteretic energies (unit: 10^3 kN mm) by FE analyses and the proposed models: (a) P1; and (b) P2.

where i indicates the load step. The differential equation of z in Eq. (11) is discretized using the Backward Euler scheme as follows:

$$\begin{aligned} z_{i+1} &= z_i + \Delta t \frac{h_{i+1}}{\eta_{i+1}} \frac{(u_{i+1}-u_i)}{\Delta t} \\ &\quad \times \left[1 - |z_{i+1}|^n \left(\gamma + \beta \cdot sgn\left(\frac{(u_{i+1}-u_i)}{\Delta t} z_{i+1}\right)\right) \nu_{i+1}\right] \frac{k_0}{F_y} \\ &= z_i + \frac{h_{i+1}}{\eta_{i+1}} (u_{i+1}-u_i) \left[1 - |z_{i+1}|^n \left(\gamma + \beta \cdot sgn\left(\frac{(u_{i+1}-u_i)}{\Delta t} z_{i+1}\right)\right)\right. \\ &\quad \left. \times \nu_{i+1}\right] \frac{k_0}{F_y}. \end{aligned} \tag{A.2}$$

In addition, the deterioration energy $\tilde{\varepsilon}$ defined in Eqs. (13) to (15) can also be expressed in an incremental form using the Backward Euler method as follows:

$$\tilde{\varepsilon}_{i+1} = \left(\tilde{\varepsilon}_{+_{i+1}} \cdot \mathrm{H}\left(u_{i+1}\right) + \tilde{\varepsilon}_{-_{i+1}} \cdot \left(1 - \mathrm{H}\left(u_{i+1}\right)\right)\right) \tag{A.3}$$

$$\tilde{\varepsilon}_{+_{i+1}} = \tilde{\varepsilon}_{+_i} + \left(1 + c_{\tilde{\varepsilon}} \cdot \mathrm{H}\left(u_{i+1} - u_{max_{i+1}}\right)\right)(1-\alpha) F_y z_{i+1} \left(u_{i+1} - u_i\right) \tag{A.4}$$

$$\tilde{\varepsilon}_{-_{i+1}} = \tilde{\varepsilon}_{-_i} + \left(1 + c_{\tilde{\varepsilon}} \cdot \mathrm{H}\left(u_{min_{i+1}} - u_{i+1}\right)\right)(1-\alpha) F_y z_{i+1} \left(u_{i+1} - u_i\right). \tag{A.5}$$

Subsequently, z should be found by solving the above incremental equations, Eqs. (A.2) to (A.5), and substituted into Eq. (A.1) to determine f_s. The details for solving the incremental equations by the Newton–Raphson method for incremental displacement $(u_{i+1} - u_i)$ are presented below.

1. *Step 1 – Calculate the evaluation function* $\Gamma\left(z_{i+1}\right)$
   The evaluation function $\Gamma\left(z_{i+1}\right)$ for the Newton–Raphson method is defined as

   $$\Gamma\left(z_{i+1}\right) = z_{i+1} - z_i - h_{i+1} a_2 \left(u_{i+1} - u_i\right) \frac{k_0}{F_y} \tag{A.6}$$

   where $a_2 = \left(1 - |z_{i+1}|^n a_1 \nu_{i+1}\right)/\eta_{i+1}$; $a_1 = \gamma + \beta \cdot \mathrm{sgn}\left(\left(u_{i+1} - u_i\right) z_{i+1}/\Delta t\right)$; $\nu_{i+1} = 1 + \delta_\nu \tilde{\varepsilon}_{i+1}$; $\eta_{i+1} = 1 + \delta_\nu \tilde{\varepsilon}_{i+1}$; and the pinching function h_{i+1} is given by

   $$h_{i+1} = 1 - \zeta_{1_{i+1}} \exp\left(-\left(z_{i+1} \cdot \mathrm{sgn}\left(\frac{(u_{i+1}-u_i)}{\Delta t}\right) - q z_{u_{i+1}}\right)^2 / \zeta_{2_{i+1}}^2\right) \times \left(1 - \exp\left(-c_h \frac{\left|u_{p_{i+1}}\right|}{u_y}\right)\right) \tag{A.7}$$

   where $z_{u_{i+1}} = \left(\nu_{i+1}(\beta+\gamma)\right)^{-1/n}$; $\zeta_{1_{i+1}} = \zeta_0\left(1 - \exp\left(-p\tilde{\varepsilon}_{i+1}\right)\right)$; and $\zeta_{2_{i+1}} = \left(\psi + \delta_\psi \tilde{\varepsilon}_{i+1}\right)\left(\lambda + \zeta_{1_{i+1}}\right)$. The definition for $u_{p_{i+1}}$ can be found in Eq. (18), and $\tilde{\varepsilon}_{i+1}$ is obtained from Eqs. (A.3) to (A.5).
2. *Step 2 – Evaluate the derivative of* $\Gamma\left(z_{i+1}\right)$ *with respect to* z_{i+1}

The derivative of the evaluation function $\Gamma\left(z_{i+1}\right)$ is expressed as follows:

$$\Gamma'\left(z_{i+1}\right) = 1 - \left(h'_{i+1} a_2 + h_{i+1} a'_2\right)\left(u_{i+1} - u_i\right) \frac{k_0}{F_y} \tag{A.8}$$

in which the derivatives of h_{i+1} and a'_2 are written as

$$h'_{i+1} = a_3\left(\zeta'_{1_{i+1}} - a_4 + a_5 \zeta'_{2_{i+1}}\right) \tag{A.9}$$

$$a'_2 = \frac{1}{\eta_{i+1}^2} \cdot \left[\eta'_{i+1}\left(1 - |z_{i+1}|^n a_1 \nu_{i+1}\right) - \eta_{i+1}\left(n|z_{i+1}|^{n-1} a_1 \nu_{i+1} \cdot \mathrm{sgn}\left(z_{i+1}\right) + |z_{i+1}|^n a_1 \nu'_{i+1}\right)\right] \tag{A.10}$$

where a_3, a_4, and a_5 are given as

$$a_3 = -\exp\left(-\left(z_{i+1} \cdot \mathrm{sgn}\left(\frac{(u_{i+1}-u_i)}{\Delta t}\right) - q Z_{u_{i+1}}\right)^2 / \zeta_{1_{i+1}}^2\right) \times \left(1 - \exp\left(-c_h \frac{\left|u_{p_{i+1}}\right|}{u_y}\right)\right) \tag{A.11}$$

$$a_4 = \frac{2\zeta_{1_{i+1}}}{\zeta_{2_{i+1}}^2}\left(z_{i+1} \cdot \mathrm{sgn}\left(\frac{(u_{i+1}-u_i)}{\Delta t}\right) - q Z_{u_{i+1}}\right) \times \left(\mathrm{sgn}\left(\frac{(u_{i+1}-u_i)}{\Delta t}\right) - q Z'_{u_{i+1}}\right) \tag{A.12}$$

$$a_5 = \frac{2\zeta_{1_{i+1}}}{\zeta_{2_{i+1}}^3}\left(z_{i+1} \cdot \mathrm{sgn}\left(\frac{(u_{i+1}-u_i)}{\Delta t}\right) - q Z_{u_{i+1}}\right)^2 \tag{A.13}$$

where $\zeta'_{1_{i+1}} = p\zeta_0 \exp\left(-p\tilde{\varepsilon}_{i+1}\right)\tilde{\varepsilon}'_{i+1}$; $\zeta'_{2_{i+1}} = \psi\zeta'_{1_{i+1}} + \lambda\delta_\psi\tilde{\varepsilon}'_{i+1} + \delta_\psi\tilde{\varepsilon}'_{i+1}\zeta_{i+1} + \delta_\psi\tilde{\varepsilon}_{i+1}\zeta'_{1_{i+1}}$; $\eta'_{i+1} = \delta_\eta\tilde{\varepsilon}'_{i+1}$; $\nu'_{i+1} = \delta_\nu\tilde{\varepsilon}'_{i+1}$; $z'_{u_{i+1}} = -\nu'_{i+1}\left(\nu_{i+1}(\beta+\gamma)\right)^{-1/n}/\left(n\nu_{i+1}\right)$; and $\tilde{\varepsilon}'_{i+1}$ is written as

$$\tilde{\varepsilon}'_{i+1} = \tilde{\varepsilon}'_{+_{i+1}} \cdot \mathrm{H}\left(u_{i+1}\right) + \tilde{\varepsilon}'_{-_{i+1}} \cdot \left(1 - \mathrm{H}\left(u_{i+1}\right)\right) \tag{A.14}$$

where $\tilde{\varepsilon}'_{+_{i+1}}$ and $\tilde{\varepsilon}'_{-_{i+1}}$ are given as

$$\tilde{\varepsilon}'_{+_{i+1}} = \left(1 + c_{\tilde{\varepsilon}} \cdot \mathrm{H}\left(u_{i+1} - u_{max_{i+1}}\right)\right)(1-\alpha) F_y \left(u_{i+1} - u_i\right) \tag{A.15}$$

$$\tilde{\varepsilon}'_{-_{i+1}} = \left(1 + c_{\tilde{\varepsilon}} \cdot \mathrm{H}\left(u_{min_{i+1}} - u_{i+1}\right)\right)(1-\alpha) F_y \left(u_{i+1} - u_i\right). \tag{A.16}$$

3. *Step 3 – Obtain the trial value of* z_{i+1}^{new}
The trial value in the Newton–Raphson method is calculated as follows:

$$z_{i+1}^{new} = z_{i+1} - \frac{\Gamma\left(z_{i+1}\right)}{\Gamma'\left(z_{i+1}\right)}. \tag{A.17}$$

4. *Step 4 – Update the trial value*
Using the trial value obtained from Eq. (A.17), z_{i+1} is updated as follows:

$$z_{i+1}^{old} = z_{i+1}, z_{i+1} = z_{i+1}^{new}. \tag{A.18}$$

5. *Step 5 – Iterate until convergence*
Iterate from Steps 1 to 4 until the following convergence condition is achieved:

$$\left|z_{i+1}^{new} - z_{i+1}^{old}\right| < \epsilon_0 \tag{A.19}$$

where ϵ_0 represents the prescribed tolerance for the convergence check.

Appendix B. Dynamic analysis of an SDOF system with the proposed Bouc–Wen class model

The incremental algorithm for the proposed Bouc–Wen class model (described in Appendix A) enables solving the equation of motion for an SDOF system given in Eq. (1) using various numerical integration schemes, such as a Runge–Kutta method. Since the Runge–Kutta method requires the equation of motion to be converted into a system of first-order ordinary differential equations, the equation of motion in Eq. (1) is transformed into a first-order, state–space equation of the form as

$$\dot{\boldsymbol{y}} = \boldsymbol{g}(\boldsymbol{y}) + \boldsymbol{f} \tag{B.1}$$

where

$$\boldsymbol{y} = \left[u, \dot{u}, z, \tilde{\varepsilon}_+, \tilde{\varepsilon}_-\right]^{\mathrm{T}} \tag{B.2}$$

$$\boldsymbol{g}(\boldsymbol{y}) = \begin{bmatrix} \dot{u} \\ -\left(c\dot{u} + \alpha k_0 u + (1-\alpha) F_y z\right)/m \\ \dot{z}\left(u, \dot{u}, z, \tilde{\varepsilon}_+, \tilde{\varepsilon}_-\right) \\ \dot{\tilde{\varepsilon}}_+(u, \dot{u}, z) \\ \dot{\tilde{\varepsilon}}_-(u, \dot{u}, z) \end{bmatrix} \tag{B.3}$$

$$\boldsymbol{f} = \left[0, \frac{F(t)}{m}, 0, 0, 0\right]^{\mathrm{T}} \tag{B.4}$$

where $\dot{z}\left(u, \dot{u}, z, \tilde{\varepsilon}_+, \tilde{\varepsilon}_-\right)$ can be found by substituting ε with $\tilde{\varepsilon}$ into Eq. (11); and $\dot{\tilde{\varepsilon}}_+(u, \dot{u}, z)$ and $\dot{\tilde{\varepsilon}}_-(u, \dot{u}, z)$ are given in Eqs. (13) and (14), respectively. Dynamic analyses for an SDOF system with the proposed model can be performed by solving Eqs. (B.1) to (B.4) using a numerical integration scheme.

References

[1] L.F. Ibarra, R.A. Medina, H. Krawinkler, Hysteretic models that incorporate strength and stiffness deterioration, Earthq. Eng. Struct. Dyn. 34 (12) (2005) 1489–1511.
[2] T. Krauthammer, N. Bazeos, T.J. Holmquist, Modified SDOF analysis of RC box-type structures, J. Struct. Eng. 112 (4) (1986) 726–744.
[3] E. Liossatou, M.N. Fardis, Residual displacements of RC structures as SDOF systems, Earthq. Eng. Struct. Dyn. 44 (5) (2015) 713–734.
[4] Y. Lu, R.S. Henry, Numerical modelling of reinforced concrete walls with minimum vertical reinforcement, Eng. Struct. 143 (2017) 330–345.
[5] Y. Zhang, X. Hu, Self-centering seismic retrofit scheme for reinforced concrete frame structures: SDOF system study, Earthq. Eng. Eng. Vib. 9 (2) (2010) 271–283.
[6] P. Sengupta, B. Li, Hysteresis modeling of reinforced concrete structures: State of the art, ACI Struct. J. 114 (1) (2017).
[7] A.S. Veletsos, N.M. Newmark, C.V. Chelapati, Deformation spectra for elastic and elastoplastic systems subjected to ground shock and earthquake motions, in: Proceedings of the 3rd World Conference on Earthquake Engineering, New Zealand, 1965.
[8] M. Ismail, F. Ikhouane, J. Rodellar, The hysteresis Bouc-Wen model, a survey, Arch. Comput. Methods Eng. 16 (2) (2009) 161–188.
[9] R. Bouc, Forced vibrations of mechanical systems with hysteresis, in: Proceedings of the Fourth Conference on Nonlinear Oscillations, Prague, Czechia, 1967.
[10] Y.K. Wen, Method for random vibration of hysteretic systems, J. Eng. Mech. Div. 102 (2) (1976) 249–263.
[11] J. Song, A. Der Kiureghian, Generalized Bouc–Wen model for highly asymmetric hysteresis, J. Eng. Mech. 132 (6) (2006) 610–618.
[12] Y.K. Wen, Equivalent linearization for hysteretic systems under random excitation, J. Appl. Mech. 47 (1) (1980) 150–154.
[13] T.T. Baber, M.N. Noori, Random vibration of degrading, pinching systems, J. Eng. Mech. 111 (8) (1985) 1010–1026.
[14] C.H. Loh, C.H. Mao, J.R. Huang, T.C. Pan, System identification and damage evaluation of degrading hysteresis of reinforced concrete frames, Earthq. Eng. Struct. Dyn. 40 (6) (2011) 623–640.
[15] P. Sengupta, B. Li, Modified Bouc–Wen model for hysteresis behavior of RC beam–column joints with limited transverse reinforcement, Eng. Struct. 46 (2013) 392–406.
[16] P. Sengupta, B. Li, Hysteresis behavior of reinforced concrete walls, J. Struct. Eng. 140 (7) (2014) 04014030.
[17] M. Pelliciari, G.C. Marano, T. Cuoghi, B. Briseghella, D. Lavorato, A.M. Tarantino, Parameter identification of degrading and pinched hysteretic systems using a modified Bouc–Wen model, Struct. Infrastruct. Eng. 14 (12) (2018) 1573–1585.
[18] B. Yu, C.L. Ning, B. Li, Hysteretic model for shear-critical reinforced concrete columns, J. Struct. Eng. 142 (9) (2016) 04016056.
[19] T. Kim, Deep Learning-Based Prediction of Seismic Responses and Losses of Nonlinear Structural Systems (Doctoral dissertation), SNU Open Repository, 2021, https://s-space.snu.ac.kr/handle/10371/175075#export_btn.
[20] F. Ikhouane, V. Mañosa, J. Rodellar, Dynamic properties of the hysteretic Bouc-Wen model, Systems Control Lett. 56 (3) (2007) 197–205.
[21] F. Ma, H. Zhang, A. Bockstedte, G.C. Foliente, P. Paevere, Parameter analysis of the differential model of hysteresis, J. Appl. Mech. 71 (3) (2004) 342–349.
[22] ACI Committee 374, Guide for Testing Reinforced Concrete Structural Elements under Slowly Applied Simulated Seismic Loads (ACI 374.2R-13), American Concrete Institute, Farmington Hills, MI, 2013.
[23] ATC-24, Guidelines for Cyclic Seismic Testing of Components of Steel Structures, Applied Technology Council, Redwood City, CA, 1992.
[24] FEMA, Interim Testing Protocols for Determining the Seismic Performance Characteristics of Structural and Nonstructural Components. FEMA 461, FEMA, Washington, DC, 2007.
[25] H. Krawinkler, F. Parisi, L. Ibarra, A. Ayoub, R. Medina, Development of a Testing Protocol for Woodframe Structures (Vol. 102), CUREe, Richmond, CA, 2001.
[26] T. Kim, O.S. Kwon, J. Song, Response prediction of nonlinear hysteretic systems by deep neural networks, Neural Netw. 111 (2019) 1–10.
[27] J. Ruiz-García, E. Miranda, Inelastic displacement ratios for evaluation of existing structures, Earthq. Eng. Struct. Dyn. 32 (8) (2003) 1237–1258.
[28] D. Vamvatsikos, C. Allin Cornell, Direct estimation of the seismic demand and capacity of oscillators with multi-linear static pushovers through IDA, Earthq. Eng. Struct. Dyn. 35 (9) (2006) 1097–1117.
[29] T. Kim, O.S. Kwon, J. Song, Deep learning-based seismic response prediction of hysteretic systems having degradation and pinching, 2022, (submitted for publication).
[30] H. Luu, I. Ghorbanirenani, P. Leger, R. Tremblay, Numerical modeling of slender reinforced concrete shear wall shaking table tests under high-frequency ground motions, J. Earthq. Eng. 17 (4) (2013) 517–542.
[31] H. Mostafaei, F.J. Vecchio, T. Kabeyasawa, Nonlinear displacement-based response prediction of reinforced concrete columns, Eng. Struct. 30 (9) (2008) 2436–2447.
[32] S. Saatci, F.J. Vecchio, Nonlinear finite element modeling of reinforced concrete structures under impact loads, ACI Struct. J. 106 (5) (2009) 717–725.
[33] F.J. Vecchio, W. Shim, Experimental and analytical reexamination of classic concrete beam tests, J. Struct. Eng. 130 (3) (2004) 460–469.
[34] M. Berry, M. Parrish, M. Eberhard, PEER Structural Performance Database User's Manual (Version 1.0), University of California, Berkeley, 2004.
[35] N.M. Kwok, Q.P. Ha, M.T. Nguyen, J. Li, B. Samali, Bouc–wen model parameter identification for a MR fluid damper using computationally efficient GA, ISA Trans. 46 (2) (2007) 167–179.
[36] D. Bertsimas, J. Tsitsiklis, Simulated annealing, Statist. Sci. 8 (1) (1993) 10–15.
[37] F.J. Vecchio, M.P. Collins, The modified compression-field theory for reinforced concrete elements subjected to shear, ACI J. 83 (2) (1986) 219–231.
[38] F.J. Vecchio, Disturbed stress field model for reinforced concrete: formulation, J. Struct. Eng. 126 (9) (2000) 1070–1077.
[39] F.J. Vecchio, Disturbed stress field model for reinforced concrete: implementation, J. Struct. Eng. 127 (1) (2001) 12–20.

[40] C. Del Vecchio, O.S. Kwon, L. Di Sarno, A. Prota, Accuracy of nonlinear static procedures for the seismic assessment of shear critical structures, Earthq. Eng. Struct. Dyn. 44 (10) (2015) 1581–1600.
[41] P.S. Wong, F.J. Vecchio, H. Trommels, Vector2 & Formworks User's Manual, second ed., University of Toronto, Canada, 2013.
[42] P.C. Jennings, G.W. Housner, N.C. Tsai, Simulated Earthquake Motions, Technical Report, Earthquake Engineering Research Laboratory, California Institute of Technology, Pasadena, CA, 1968.
[43] S. Saatci, F.J. Vecchio, Finite element analysis of shear-critical reinforced concrete beams under impact loading, in: Proceedings of the 6th ASIA-Pacific Conference on Shock and Impact Loads on Structures, Perth, Australia, 2005.
[44] M.R. Hossain, M. Ashraf, J.E. Padgett, Risk-based seismic performance assessment of yielding shear panel device, Eng. Struct. 56 (2013) 1570–1579.
[45] C.L. Ning, Y. Cheng, X.H. Yu, A simplified approach to investigate the seismic ductility demand of shear-critical reinforced concrete columns based on experimental calibration, J. Earthq. Eng. 25 (10) (2021) 1958–1980.